

Response of the Separated Flow over an Airfoil to Short-Time Actuator Bursts

Xuanhong An¹†, and David R. Williams¹

¹Department Mechanical, Materials and Aerospace Engineering, Illinois Institute of Technology, IL, 60616, USA

(Received xx; revised xx; accepted xx)

The separated flow response to single and multiple burst mode actuation over a 2-D airfoil at 12° angle of attack was studied experimentally. For the single-burst actuation case, surface pressure signals were correlated with the flowfield observations of the roll-up and convection of a large-scale vortex structure that follows the actuator burst input. A spatially localized region of high pressure occurs below and slightly upstream of a “kink” that forms in the shear layer, which is responsible for the lift reversal that occurs within $2.0t^+$ after the burst signal was triggered. Proper orthogonal decomposition of the single-burst flow field shows that the time-varying coefficients of the first two modes correlate with the negative of the lift coefficient and pitching moment coefficient. The dynamic mode decomposition (DMD) of the single-burst flow field data identified the modes related to the kinetic energy growth of the disturbance. The mode with the largest growth rate had a Strouhal number close to that associated with the separation bubble dynamics. However, when multiple bursts are used to control the separation, the interactions between the bursts were observed which depend on the time intervals between the bursts. The convolution integral and DMD were performed on the multi-burst flow field datasets. The results indicate that the nonlinear burst-burst interaction only affects the reverse flow strength within the separation bubble, which is related to the main trend of the lift. On the other hand, the linear burst-burst interaction contributes to the high-frequency lift variation associated with the bursts.

Key words: Authors should not enter keywords on the manuscript, as these must be chosen by the author during the online submission process and will then be added during the typesetting process (see <http://journals.cambridge.org/data/relatedlink/jfm-keywords.pdf> for the full list)

1. Introduction

The application of active flow control (AFC) methods to reattach separated flows has attracted a lot of attention, due to its potential to enhance the performance of machines in a wide range of applications, such as, aircraft flight efficiency, pressure recovery in diffusers, road vehicle drag reduction and control in gusting flow, noise generation from propellers, and power output from wind turbines. In general, on nominally two-dimensional airfoils AFC methods are capable of performance enhancement in one of two ways. The first is to prevent flow separation at high angles of attack by using pre-set actuation. Delaying the onset of flow separation enables lower takeoff and landing speeds

† Email address for correspondence: xan2@hawk.iit.edu

for aircraft, and enables better controllability at high angle of attack. When the AFC actuator runs continuously, then we refer to this approach as steady separation control. The second method deals with AFC when the flow or the vehicle has a flow separation that is time-varying. When unsteadiness is involved then the control effect often needs to be synchronized with the changing external flow or changing vehicle trajectory. We refer to the second method as unsteady separation control. Unsteady separation control allows the "reattachment length" to be varied with time, so that forces and moments can be applied on the airfoils without changing the pitch attitude or using moving the control surfaces. Similarly, alleviating the unsteady flow separation due to some rapid maneuvers can also be achieved. Unsteady separation control with AFC has proven to be challenging to implement, because of the nonlinear behavior of the separated flow and the significant time delays between the onset of actuation and the flow response.

Understanding the dynamic behavior of separated flow response to actuator input will benefit the active flow control system design in at least two ways. First, it provides more insight into the flow physics behind the actuation effectiveness, which will benefit the actuator design for both steady and unsteady separation control. Second, a better understanding of the interaction between the separated flow response and the actuator input could benefit the development of low-order models of the aerodynamic loads to the time-varying actuator input. Modeling the load response to actuator input is essential for the real-time controller design for active flow control systems, especially for the unsteady separation control. Some important earlier investigations into the behavior of separated flow response to actuator input are discussed next.

Raju *et al.* (2008) investigated the steady state behavior of separated flow over an NACA 4418 airfoil and identified three distinct time scales associated with the separated flow. The time scales are associated with the Kelvin-Helmholtz shear layer instability, the separation bubble, and the wake. They reported that continuous harmonic actuation at the separation bubble frequency gives the maximum lift recovery, but we expect any type of AFC actuation is likely to excited all three instabilities. We also expect interactions between the different modes of instability will be important. For example, by conducting experiments on circular cylinders with different diameters, Prasad & Williamson (1996) reported that the shear layer instability frequency, f_{SL} , is related to the wake frequency, f_{wake} as $f_{SL} = 0.0235Re^{0.67}f_{wake}$. For an airfoil, the wake frequency is expressed as $St = \frac{f_{wake} \cdot c \cdot \sin(\alpha)}{U_\infty}$ (Strouhal 1878; Fage & Johansen 1927), where c is the chord length, α is the angle of attack and U_∞ is the freestream speed. The value of the separation bubble frequency f_{sep} scales as $f_{sep} \sim U_\infty/L_{sep}$ by Raju *et al.* (2008), where L_{sep} is characteristic length of the separation region.

Instead of using continuous harmonic excitation with the actuator, a different approach to study the dynamics of the separated region response to the actuation is to use an impulse-like disturbance to perturb the separated flow region, and then follow the development of the disturbance. When the system is linear and time invariant, the impulse response can be used in a convolution integral to predict the response from any arbitrary input. The impulse-like disturbances excite a broad spectrum of modes within the separated flow, which can trigger multiple instabilities (Monnier *et al.* 2016). Amitay & Glezer (2002a) conducted experiments on a stalled wing using this approach, and identified an initial reversal in the lift increment following a short burst (single-burst) input from a synthetic jet actuator prior to the lift increasing. The lift reversal typically occurs within the first 1.5 convective times, and it turns out to be a key feature of the transient response at the onset of actuation. The lift reversal is a characteristic of non-minimum phase behavior of a system. From a control theory perspective, this means the

system will have an inherent time delay that will limit the bandwidth of control, and there will be an upper limit to how fast the lift can be controlled. In fact, it was shown by Kerstens *et al.* (2011), that this time delay was responsible for limiting the bandwidth in the gust alleviation experiments on a three-dimensional wing.

In addition, Monnier *et al.* (2016) reported that the circulatory force on a wing in response to an impulse-like pitching motion also follows the same lift reversal behavior as the AFC actuators (e.g. synthetic and burst-blowing jets). Therefore, the similar inherent time delay (lift reversal) observed with the pneumatic actuators also exists when the wing is mechanically moved. Under this circumstance, faster actuators alone will not make the flow respond faster. In fact, Williams & King (2018) reported that the inherent time delay (lift reversal) is due to the nature of the separated flow and independent of the actuators. Thus, to increase the speed at which the forces can be controlled, a deeper understanding of the fluid dynamics responsible for the non-minimum phase (lift reversal) behavior of the separated flow system is required.

The lift enhancement that follows the lift reversal (Amitay & Glezer 2006) for the single-burst actuation should also be related to the three instabilities associated with the separated flow region. The instabilities contained in the separated flow are the mechanisms by which the high-energy external flow from the freestream becomes transported into the separation region. These instabilities are also closely related to the lift enhancement maximization for continuous actuation. In fact, Raju *et al.* (2008) suggested that the maximum lift gain, relative to the non-actuation baseline case, will be achieved by the harmonic actuation running at the vicinity of the subharmonics of the separation bubble frequency.

However, it is unlikely that the separated flow response to a single burst is linear. Linear systems have the additive property $f(x + y) = f(x) + f(y)$ and the homogeneous property $f(ax) = af(x)$. The homogeneous property of linear systems is not followed by the separated flow. For example, An *et al.* (2016) showed that when the amplitude of the input pulse is doubled, the response amplitude is not doubled. The nonlinear response behaves like a static nonlinearity with a square root dependence.

Finite-length sequences of actuator bursts fall between continuous steady state actuation and single burst actuation. By assembling a finite sequence of single-burst actuation signals with specific spacing in time between them, we can observe the transition from a pulse response to the steady state behavior of the separated flow.

Amplitude modulation of the continuous burst actuation is often used for flow separation control, in which unsteady aerodynamic loads occur (Kerstens *et al.* 2010) (Kerstens *et al.* 2011) (Williams *et al.* 2015). But this further complicates the dynamic response of the separated flow to the actuation comparing to the single-burst actuation (An *et al.* 2016). Therefore, studying on the separated flow response to the continuous actuation will benefit the actuation effectiveness as well as the low-order modeling approach for the real-time flow control applications. In the current work, we employed multi-burst actuation with specific burst-burst spacing in time to study the continuous actuation. Unlike the continuous burst actuation, the multi-burst actuation can be initialized from the baseline state and ended within a limited time. Thus, besides the fully developed burst-burst interaction (the same as in the continuous actuation case), it is able to capture both the initial transition during the first several bursts and the relaxation stage after the last burst.

In this paper, a study of the flow physics behind the single-burst, multi-burst actuation is carried out. Detailed particle image velocimetry (PIV), pressure and force measurements were conducted. Dynamic mode decomposition (DMD) was performed on the flow field data to extract their dynamic characteristics. The remaining of this paper

is organized as follows, the detailed experimental setup is described in section 2. The investigation of lift reversal, POD analysis and instability analysis following the single-burst actuation is carried out in section 3. The burst-burst interaction in the multi-burst actuation is studied in section 4. The conclusions are given in section 5.

2. Experimental Setup

The experiments were conducted in the Andrew Fejer Unsteady Flow Wind Tunnel at Illinois Institute of Technology. The wind tunnel has cross-section dimensions $600\text{mm} \times 600\text{mm}$. The right-hand coordinate system is defined with the origin at the leading edge of the wing and the x-axis in the flow direction, the y-axis pointing upward, and the z-axis pointing in the direction of the left side of the wing. A nominally two-dimensional NACA0009 wing with a wingspan $b = 596\text{mm}$ and chord length $c = 245\text{mm}$ was used as the test article that is shown in figure 1. The freestream speed was $U_\infty = 3\text{m/s}$, corresponding to a convective time $t_{convect} = c/U_\infty = 0.082\text{s}$. Dimensionless time t^+ is normalized by the convective time so that $t^+ = t/t_{convect}$. The chord-based Reynolds number is $Re_c = 49,000$. The angle of attack of the wing was fixed at $\alpha = 12^\circ$, at which the flow is fully separated on the suction side of the airfoil.

Eight piezoelectric (zero net mass) actuators were installed in the leading edge of the wing. The slots of the actuators were located $0.05c$ from the leading edge with an exit angle of 30 degrees from the tangent to the surface on the suction side of the wing. The dimension of each actuator orifice slot is $2\text{mm} \times 40\text{mm}$.

Surface pressure measurements were made with All-Sensors D2-P4V Mini transducers built into four chord-wise locations on the wing. The pressure range for these sensors is ± 1 inch of water. The four pressure sensors are shown in figure 1 as PS1 – PS4, and the corresponding pressure coefficient measurements will be denoted as $C_{P1} - C_{P4}$ in the rest of this paper. Forces and moments were measured with an ATI, Inc. model Nano-17 force balance located inside the model at 30% of the chord, which is also the center of gravity of the wing. The reference point of the pitching moment is located at 25% of the chord.

Particle Image Velocimeter (PIV) flow field measurements were obtained in the x,y plane located at $z=0.19b$ away from the centerline (indicated by the orange line in figure 1). The PIV data window in the x,y plane is shown in figure 2 with green color. The small red circle denotes the streamwise location of the actuators and the black dots are the locations of the pressure sensors. The time interval between the phase-averaged PIV measurements is 0.005s ($0.0625t^+$), which resulted in 800 phases covering 4s ($50t^+$). The phase averaging was done by averaging 100 flow field images for each phase. The initial (reference) phase corresponded to the beginning of the actuator burst signal.

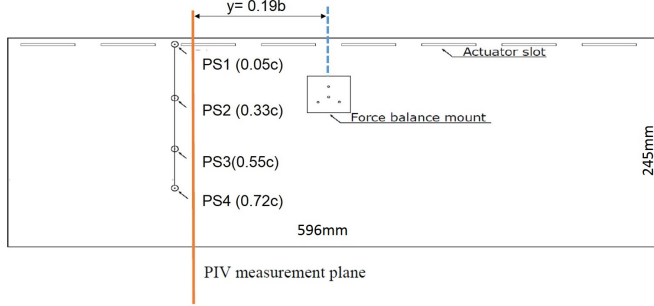


Figure 1: Plan view of the wing with NACA 0009 profile. Pressure sensor, force balance, and actuator locations are shown.

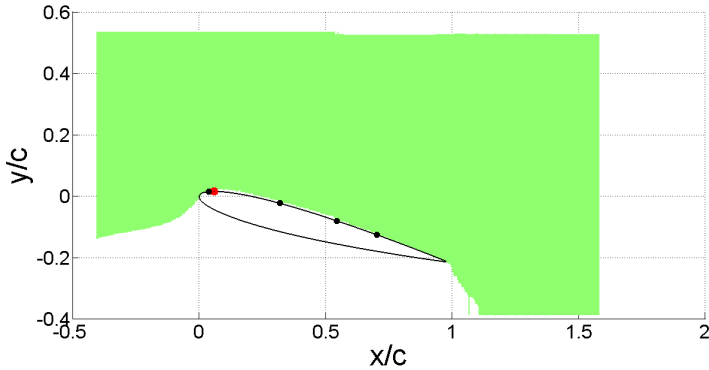


Figure 2: Side view of the wing and the PIV measurement window. Pressure sensor locations are shown by the black dots, and the actuator locations are shown by the red dot.

To produce the maximum exit jet velocity, the zero net mass actuators are operated at their mechanical resonance frequency, $f_r = 400\text{Hz}$ with a pulse width of $\Delta t_p = 0.03125t^+$, and 60 Volts (V) amplitude. A second square wave signal was superposed on the 400 Hz carrier signal to create the ‘burst signal’. The burst signal width is $\Delta t_b = 0.125t^+$. Therefore, the actual input signal to the actuators is a short burst signal containing 4 high-frequency (400Hz) pulses, the amplitude of the input signal $A = 60V$ for all the cases in the current research (figure 3). The peak exit jet velocity measured with a hot-wire anemometer at the actuator exit is 4.9m/s corresponding to the peak $C_\mu = \frac{\rho V_{jet}^2 A_{jet}}{0.5 \rho U_\infty^2 cb} = 0.01$, where V_{jet} is the peak velocity of the actuation jet, A_{jet} is the opening area of the actuators, ρ is the air density, U_∞ is the freestream velocity, c is the chord length of the wing, and b is the wingspan.

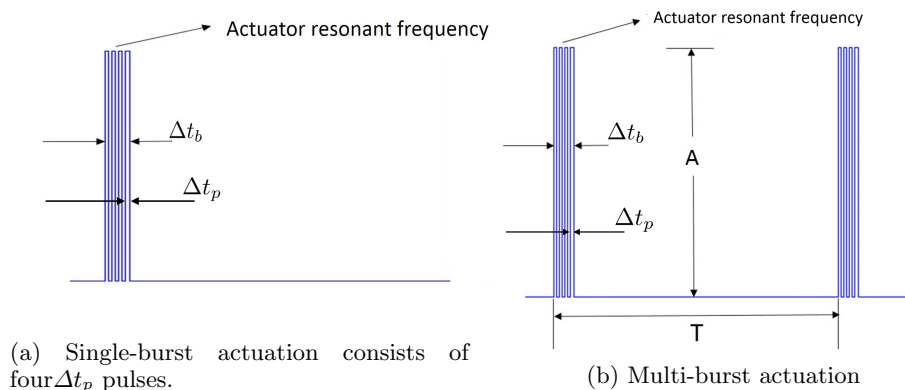


Figure 3: Input signal to the actuators.

3. Single-burst Actuation

The single-burst actuation consists of a sequence high-frequency pulses as shown in the diagram in figure 3a. The corresponding velocity field and streamline response to the single-burst actuation is shown at different instants in figure 4. The color corresponds to velocity magnitude. Figure 5 shows the lift coefficient $C_L = \frac{L}{0.5\rho U^2 cb}$ (blue) and pitching moment coefficient $C_M = \frac{M}{0.5\rho U^2 c^2 b}$ (red) response, where L is the lift force and M is the pitching moment. Positive M corresponds to a nose-up pitching moment. The vertical dashed black lines in figure 5 correspond to the instantaneous flow fields shown in figure 4. Both C_L and C_M decrease immediately following the single-burst signal, which can be seen from the time series C_L , C_M data plotted in figure 5a to figure 5c. Similar lift reversal phenomenon was identified first by Amitay & Glezer (2002b). Since then the effect has been observed by numerous investigators, (Woo *et al.* June 2008; Brzozowski *et al.* 2010; Woo *et al.* 2009), and is now an established feature of the separated flow dynamics.

Referring to the velocity field prior to the burst in figure, the baseline flow on the suction side is fully separated at $\alpha = 12^\circ$ angle of attack (figure 4a). The single-burst actuation was initiated at $0t^+$ and lasted for $0.12t^+$. The beginning of the reattachment process can be seen at $0.5t^+$ at $x/c = 0.2$ from the leading edge (figure 4b). The reattachment produces a “kink” in the shear layer that divides the new ‘reattached’ flow from the ‘old’ separated flow region. The reattached region grows with time as the kink convects downstream from the leading edge towards the trailing edge as shown in figure 4b to figure 4d. The maximum flow reattachment occurs when the kinked region of the shear layer reaches the trailing edge at $2.8t^+$ (figure 4d). The lift coefficient is also a maximum at this time, which agrees with Rival’s observations (Rival *et al.* 2014). After $4t^+$, the lift coefficient begins to decrease as the flow field gradually relaxes to its original baseline state. This relaxation process is exhibited in figure 4e and figure 4f, and it takes about $10t^+$. Brzozowski *et al.* (2010) described much of the same behavior when using combustion-based pulsed actuators on an NACA 4415 cambered wing.

Figure 5c shows that both C_L and C_M reach their minimum at $1.4t^+$ before they start their climb to the maximum increments. The C_L reaches its maximum at $2.8t^+$ (figure 5d), which is consistent with the flow field measurement shown in figure 4d where the flow reattachment length also reaches its maximum. The maximum C_L increment is about 30% of its undisturbed baseline value.

In contrast to the C_L behavior there is no significant increase in C_M above the baseline

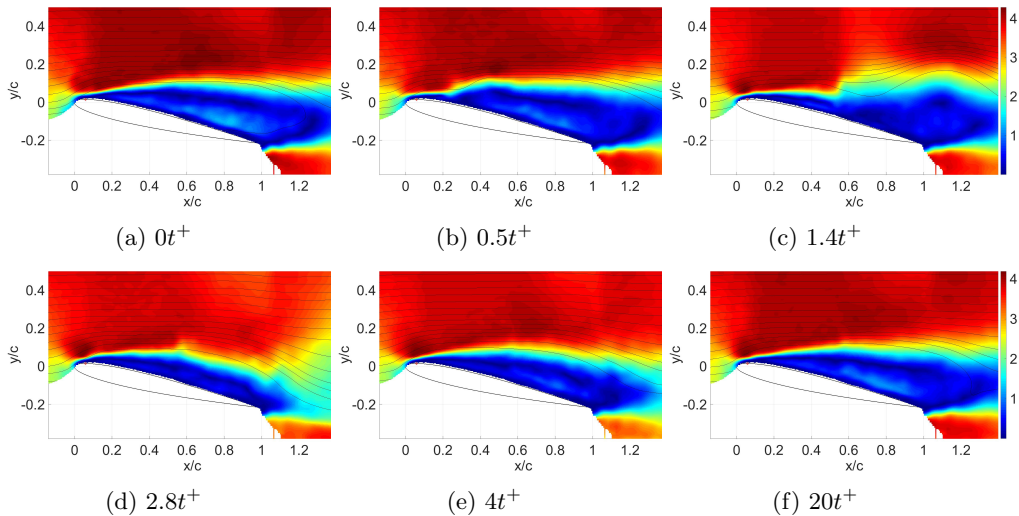


Figure 4: Phase-averaged velocity magnitude ($\sqrt{U^2 + V^2}$) and streamline time sequence plots following a single-burst actuation that was triggered at $0t^+$. The color indicates the velocity magnitude and the black lines are showing the streamline. The red circle on the leading edge denotes the streamwise location of the actuators.

(figure 5). At $4t^+$ later, as can be seen in figure 5e and figure 5f both C_L and C_M start to return to their baseline undisturbed condition, which is also consistent with the flow field (figure 4e and figure 4f). A more detailed discussion about the C_L , C_M reversal and increment will be provided in the following section by using pressure measurement and vortex structure.

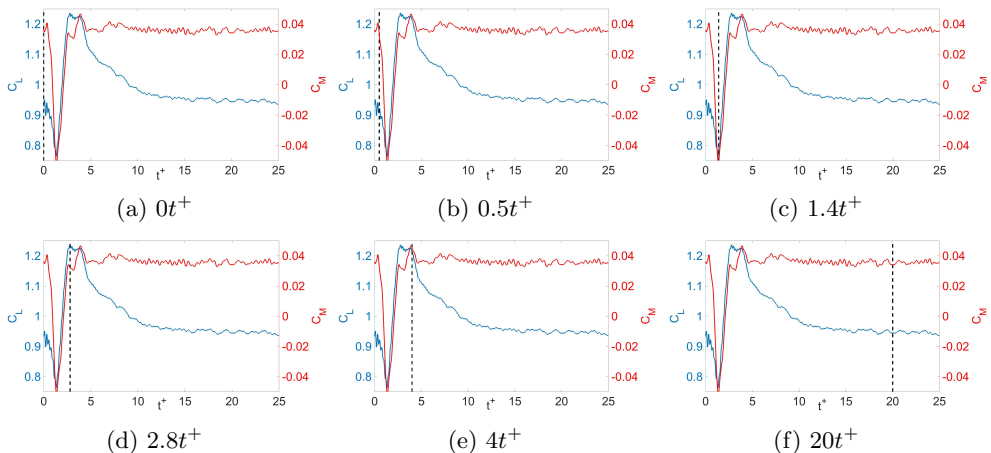


Figure 5: Phase-averaged C_L (blue) and C_M (red) variation following a single-burst actuation that was triggered at $0t^+$. The solid blue line denotes C_L , the solid red line denotes C_M and the dashed black line indicates the time instant correlated to each flow field in figure 4.

3.1. The mechanism of C_L , C_M reversal

The mechanism behind the lift and pitching moment reversals is important to understand, because it is the reason for the non-minimum phase behavior that limits control bandwidth. By examining the vortex structure and surface pressure evolution, we intend to gain some insight into the physics of the lift and pitching moment reversal. The methodology here is that we will first relate the lift and pitching moment to the pressure, and then link the pressure to the flow field evolution.

The time-varying increments ΔC_L , ΔC_M and ΔC_P are shown in figure 6. Here, " Δ " denotes the disturbed value relative to the baseline. Note that the vertical axis on figure 6b is " $-\Delta C_P$ " for a easier comparison with ΔC_L and ΔC_M . The pressure response to the short burst actuation was investigated at four chordwise locations. It can be seen in figure 6 that the pressure at locations PS2, PS3, and PS4 follow a similar trend following a pulse disturbance from the actuator. There is an approximately $0.6t^+$ constant time delay between the minima in the pressure sensor signals due to the convection of the disturbance. The first pressure signal on PS1 does not follow the same pattern as the other pressure sensors, because it is upstream of the actuator. The pressure data variation will be discussed in more detail later associated with the vortex structure.

The trend of ΔC_L data follows approximately the sum of all the pressure measurements. A comparison of ΔC_L normalized by the maximum lift coefficient increment ΔC_{Lmax} (blue) and the normalized value of the sum of the pressure measurements is plotted in figure 7a (red). The trend of the pitching moment closely tracks C_{P4} (figure 7b), which is close to the trailing edge. This is because the moment arm of PS4 is the largest relative to the reference point of the moment measurement.

Up to now, we can conclude that the C_L and C_M reversals are a consequence of the surface pressure reversal following the initial actuator input. Next, we will relate the time-varying surface pressure to the vortex structure, so that we obtain a complete picture of how the flow field evolution contributes to the C_L , C_M reversal.

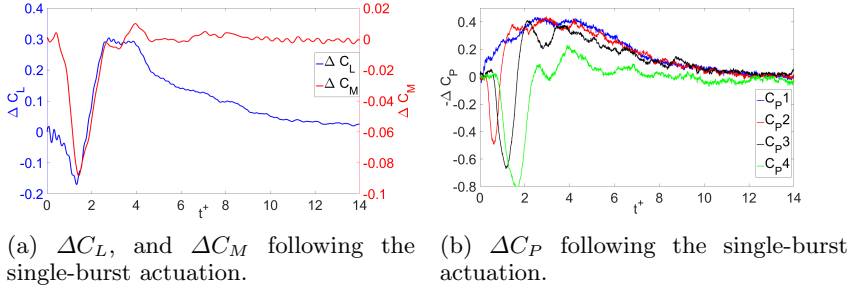


Figure 6: Lift coefficient increment and pitching moment coefficient increment measured by the force transducer, and pressure coefficient increments measured by the four pressure sensors.

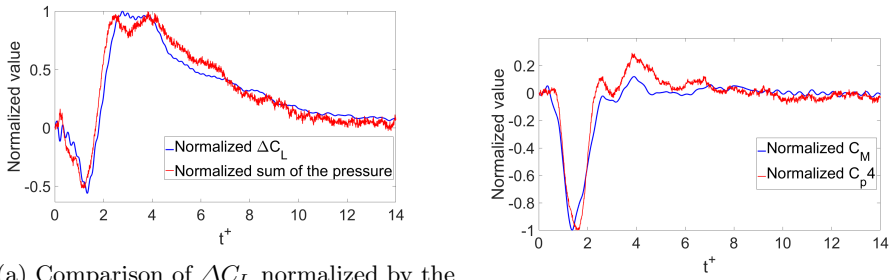


Figure 7: Lift and moment coefficient increments normalized by their respective maxima.

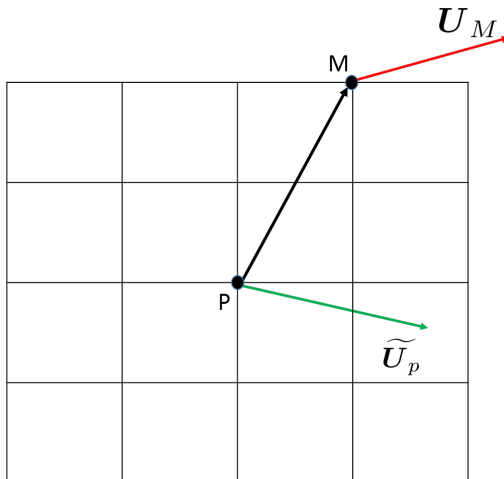
To investigate the vortex structure associated with the lift reversal, the PIV data was analyzed using a method following Graftieaux *et al.* (2001). A Galilean invariant vortex strength Γ in the flow was calculated that uses the local swirling velocity and the spatial vector relative to the center point of the computational region. To reduce the noise in the measured flow field, a local averaging method was used.

$$\Gamma(p) = \frac{1}{N} \sum_S [\mathbf{PM} \wedge (\mathbf{U}_M - \widetilde{\mathbf{U}}_p)] \cdot \mathbf{Z} \quad (3.1)$$

where \mathbf{PM} is the spatial vector from the center point P of the computational area to each individual point M surrounding P in the computational area S . N is the number of points in the surrounding area. \mathbf{U}_M is the velocity at the point M . $\widetilde{\mathbf{U}}_p$ is the mean velocity in the area S and \mathbf{Z} is the unit vector normal to the measurement plane. In the 2-D case, Eq. 3.1 becomes

$$\Gamma(p) = \frac{1}{N} \sum_S [\mathbf{PM} \wedge (\mathbf{U}_M - \widetilde{\mathbf{U}}_p)] \quad (3.2)$$

The computational region of Γ at the spatial point P is sketched in figure 8.

Figure 8: The sketch of the Γ computational area.

To better visualize the vortex structure, the Galilean invariant Λ_2 criterion (Jeong & Hussain 1995) was used to identify the vortex boundary. The vortex strength Γ is only shown inside the vortex boundary defined by Λ_2 . Taking the gradient of Navier-Stokes equations, the symmetric part without unsteady and viscous effects is

$$\Omega^2 + S^2 = -\frac{1}{\rho} \nabla (\nabla P) \quad (3.3)$$

where $S = (J + J^T)/2$, $\Omega = (J - J^T)/2$ and J is the velocity gradient tensor. The tensor $\Omega^2 + S^2$ is the corrected Hessian of pressure. The vortex core can be defined as a connected region with two negative eigenvalues ($\Lambda_2 < 0$) of tensor $\Omega^2 + S^2$. In our case, ($\Lambda_2 < -100$) is used to reduce the number of the small vortices that are caused by the turbulence and measurement noise.

The vortex structures in figure 9 are plotted at the ‘critical’ instants that include the minimum C_L , maximum C_L , the downwash (which will be discussed in more detail later) acting on each pressure sensor and the original baseline flow. The vortex structure at $0t^+$ (figure 9a) shows a group of clockwise rotating vortices (blue) above the airfoil denoting the separated boundary layer, and some counterclockwise rotating vortices (red) at the vicinity of the trailing edge indicating the trailing-edge vortex (TEV). As shown in figure 9b, the single-burst actuation cuts the shear layer into two parts. The upstream part forms a new leading-edge vortex that bonds to the leading edge. We call this vortex the newly established leading-edge vortex (NELEV). The downstream portion of the shear layer rolls up into another vortex which eventually detaches from the airfoil. The previously discussed ‘kink’ in the shear layer is at the interface between the two vortex structures. The size of the downstream vortex grows continuously before it completely detaches from the airfoil (figure 9c to 9e). This vortex is referred to as the detached leading-edge vortex (DLEV). At $2.8t^+$ (figure 9g), both the DLEV and the counter-clockwise rotating TEV have detached from the wing. The separation bubble becomes smaller than the baseline separated flow, and the resulting flow leaves the trailing edge smoothly. The reattachment point reaches the trailing edge at this time, and the lift increment reaches its maximum as previously shown in figure 4d and figure 5d. Finally, as expected, at $20t^+$ after the actuation (figure 9h) the flow has returned to the original baseline state.

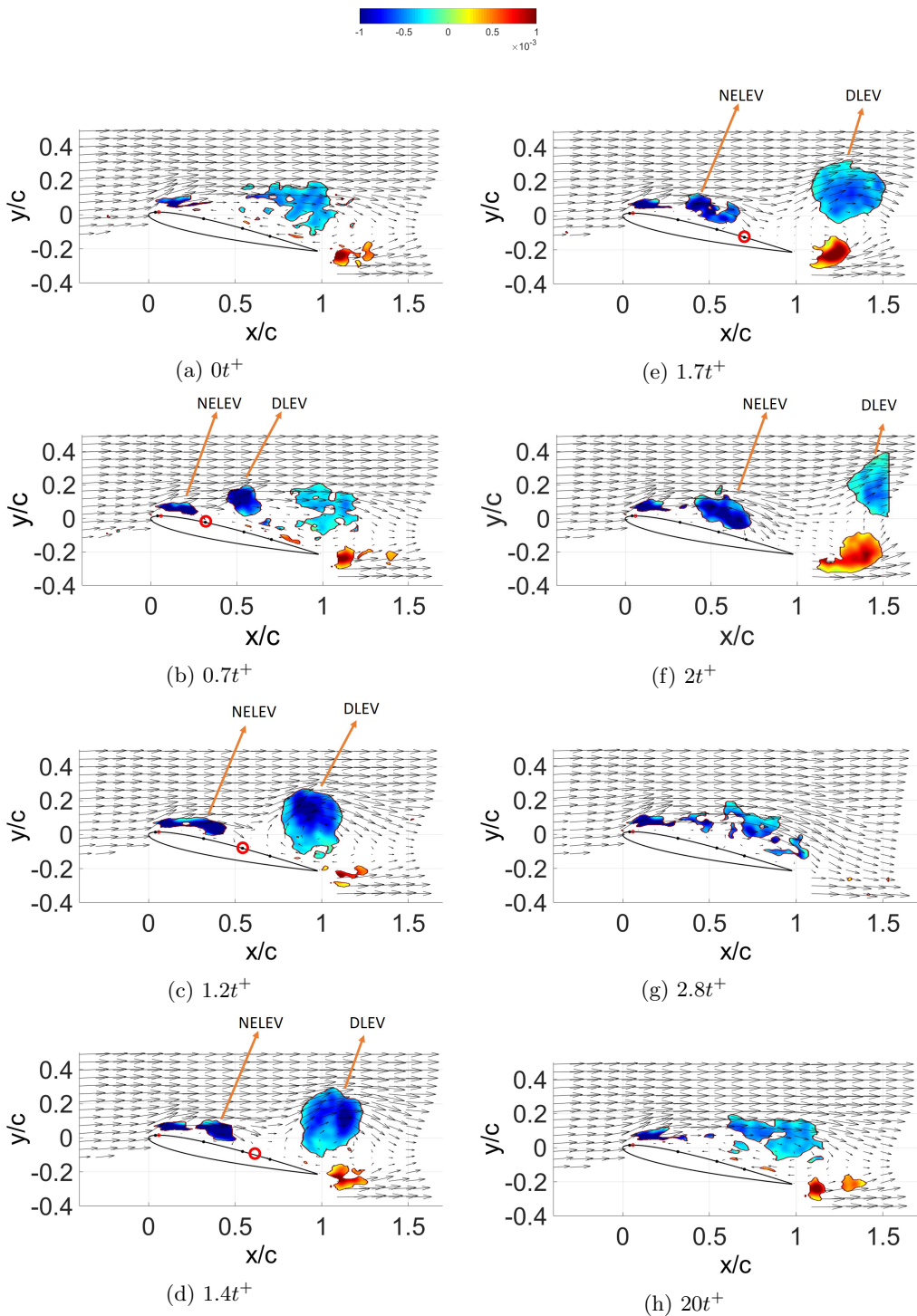


Figure 9: Vorticity maps and velocity vectors following a single burst from the actuator. The red circles denote the location where the downwash impacts the wing. The red dot close to the leading-edge indicates the location of the actuators, and the black dots show the location of the pressure sensors. The plots from a to h represent baseline ($0t^+$), maximum pressure on PS2 ($0.7t^+$), maximum pressure on PS3 ($1.2t^+$), minimum C_L ($1.4t^+$), maximum pressure on PS4 ($1.7t^+$), vortices shed from the wing ($2t^+$), maximum C_L ($2.8t^+$) and the baseline ($20t^+$).

The NELEV vortex structure in figure 9 induces a downward flow that correlates with the pressure reversal at each pressure sensor following the burst actuation. The location, where the downwash acts on the suction side surface of the wing is shown in figure 9 b-e with red circles. At $0.7t^+$ after the firing of the burst (figure 9b), the downwash flow is acting on the pressure sensor 2, and this pressure sensor is showing maximum pressure reading (figure 6). The peak in the pressure reversal occurs at pressure sensors 3 and 4 (figure 9c and figure 9e) at slightly later times as the NELEV convects downstream towards the trailing edge of the airfoil.

Therefore, by combining the results of the ΔC_L and ΔC_M measurements, the surface pressure measurements (figure 6 and figure 7a) and the vortex structure inside the flow field (figure 9), we conclude that the NELEV induces a downwash velocity that acts on the suction side of the airfoil and moves downstream. This downwash contributes to a local pressure reversal and as a consequence, the local pressure reversal leads to the lift and pitching moment reversal following the single-burst actuation. It is also worth pointing out that it takes about $2t^+$ (figure 9f) for the leading edge vortex to detach and convect downstream into the wake, which leads to the ΔC_L increase. But it takes about $10t^+$ for the "re-separation" process (figure 4e to figure 4f) to occur, which is responsible for the C_L returning to its initial condition.

3.2. Proper Orthogonal Decomposition (POD) of the flow field

Next we apply the Proper Orthogonal Decomposition (POD) to the transient case of the single burst actuation to gain additional insight into the modes that are responsible for the lift and pitching moment reversal. In a similar experiment, Monnier *et al.* (2016) reported that the temporal coefficient of the second Proper Orthogonal Decomposition (POD) mode correlates with the negative of the lift coefficient variation following a single-burst input. The POD method can reduce a large number of interdependent variables to a much smaller number of independent modes, while retaining as much as possible the variation in the original variables (Kerschen *et al.* 2005).

$$v(x, t) = \sum_{i=1}^{\infty} a_i(t) \phi_i(x) \quad (3.4)$$

In Eq. 3.4 a_i is the time-dependent temporal coefficient and $\phi_i(x)$ is the POD basis function. Singular Value Decomposition (SVD) (Kerschen *et al.* 2005) is performed on both horizontal and vertical velocity components obtained from the PIV measurements.

For any given ($m \times n$) matrix X

$$X = USV^T \quad (3.5)$$

where U is an ($m \times m$) orthonormal matrix containing the left singular vectors, S is a ($m \times n$) pseudo-diagonal and semi-positive definite matrix with diagonal elements δ_i , and V is an ($n \times n$) orthonormal matrix containing the right singular vectors. There are physical meanings for each term from the SVD. The matrix U represents the spatial distribution of velocity within each POD mode, V contains the temporal coefficients for each mode, and the pseudo-diagonal elements of S denote the energy level for the modes, in which the energy is descending with increasing of the mode number.

The energy contained in each mode is normalized by the first mode's energy and plotted in figure 10. It shows that about 84% of the disturbed flow energy (with mode 0 subtracted from the flow field) is contained in mode 1 and mode 2, which means that mode 1 and mode 2 can reconstruct a flow field containing most of the energetic structures in the actual disturbed flow field.

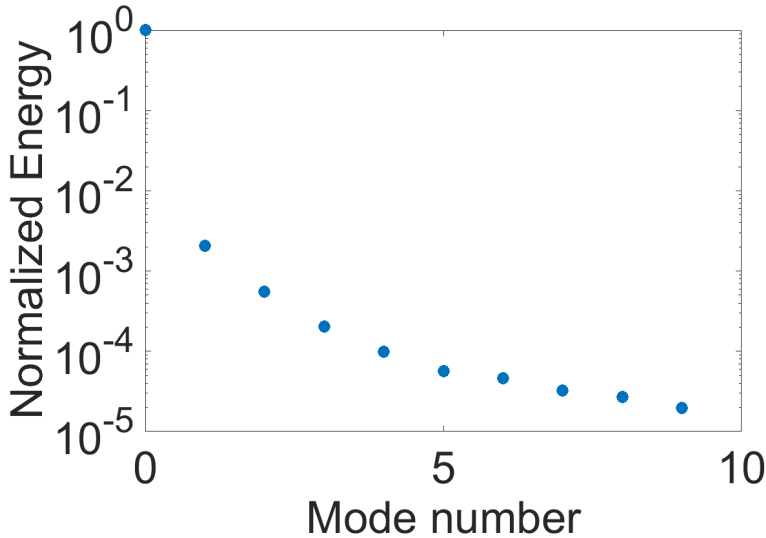


Figure 10: Energy distribution versus POD mode number.

The corresponding basis functions and the temporal coefficients for the first three modes are plotted in figure 11. Mode 0 (figure 11a) shows the baseline separated flow. And figure 11b shows that this mode almost remains unchanged with time. The temporal coefficient of this mode is always above 0 which means the velocity vector direction in figure 11a will not be flipped. Mode 1 shown in figure 11c is related to a clockwise rotating vortex above the trailing edge and the backward flow that causes the boundary to reattach. The temporal coefficient (figure 11d) of this mode goes negative after the burst is fired, which implies that the velocity vectors in the spatial mode flip their directions. Mode 2 shown in figure 11e indicates a counterclockwise rotational flow pattern upstream of the trailing edge and a clockwise rotational vortex which bonds to the mid chord on the suction side. This flow structure produces a downwash impinging on the upper surface of the wing close to the pressure sensor 4. The temporal coefficient of this mode (figure 11f) goes above 0 following the burst, which preserve the direction of the velocity vectors in figure 11e. This implies that mode 2 is related to the C_L and C_M reversal. Next, we will exhibit the relation between the C_L and C_M and the POD modes.

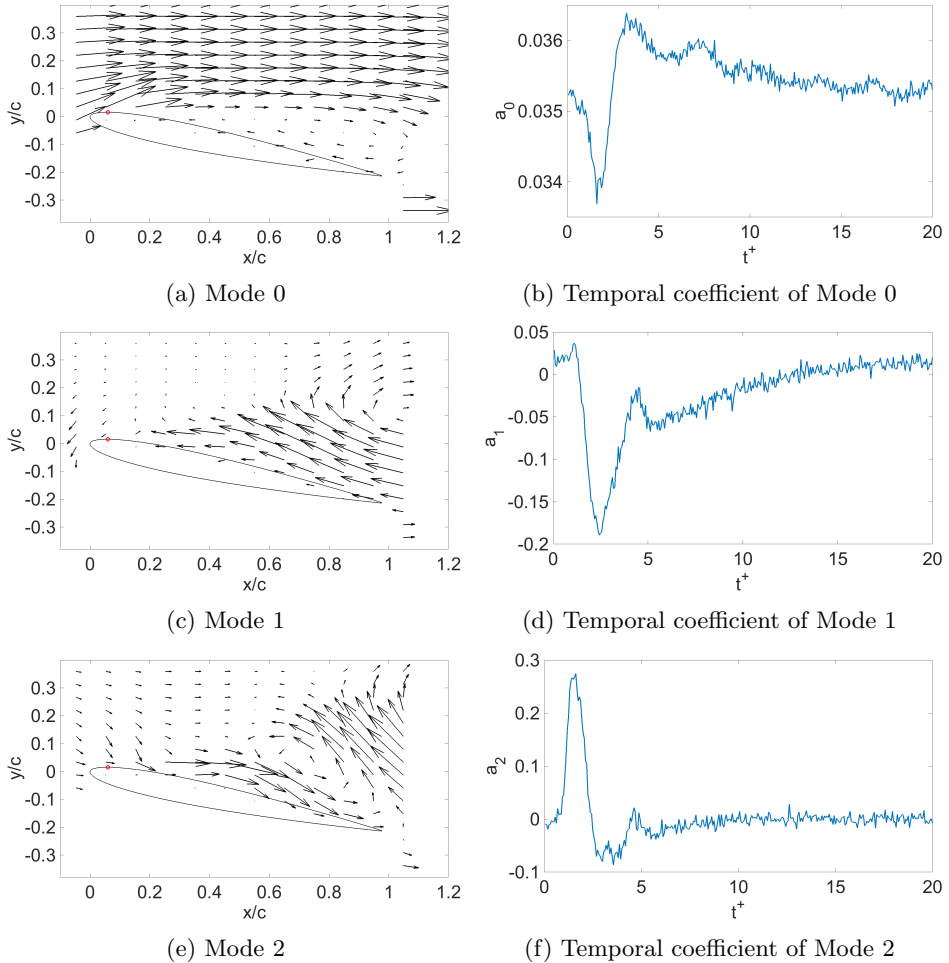


Figure 11: Comparison of the first four spatial POD modes and their corresponding temporal coefficients.

The sum of the temporal coefficients of mode 1 and mode 2 is plotted in figure 12a. Comparing the ΔC_L (baseline C_L subtracted from the transient C_L) to $a_1 \cdot \delta_1 + a_2 \cdot \delta_2$, the combined temporal coefficient tracks the negative ΔC_L quite well (especially for the lift reversal), other than the second mode alone, reported by Monnier *et al.* (2016). The negative temporal coefficient of mode 2 is closely tracking the measured ΔC_M , since this mode represents the downwash acting on pressure sensor 4. This can be seen in figure 12b.

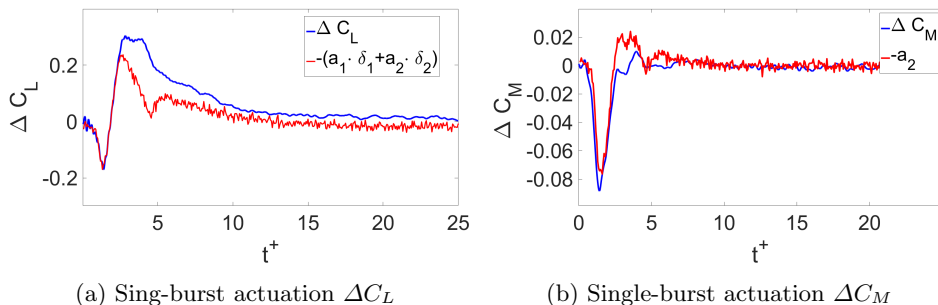


Figure 12: Comparison of aerodynamic loads and time varying coefficient of POD modes, (a) lift coefficient, (b) pitching moment coefficient.

3.3. Stability Analysis of the flow field

According to Raju *et al.* (2008) there are three instability mechanisms within the separated flow that govern its response to disturbances; namely, the Kelvin-Helmholtz shear layer, the separation bubble, and the wake instability. The actuator injects a small-amplitude, spatially-localized disturbance into the separating shear layer. In the single pulse case, the disturbance would have a broad spectrum. Based on the findings by Raju *et al.* (2008) we surmise that the initial growth of the disturbance will follow linear dynamics that result from one or more instabilities. Nonlinear interactions and saturation of the disturbance will ultimately limit the maximum amplitude of the disturbance, which is reflected in the lift response.

To investigate the possibility of linear instability mechanisms controlling disturbance development within the separated flow, the single-burst disturbance is studied utilizing the dynamic mode decomposition (DMD) (Rowley *et al.* 2009) (Schmid 2010) based on the kinetic energy within the PIV window. The single-burst actuation triggers a transient disturbance within the flow field, which is not a typical application of DMD (Rowley *et al.* 2009). Therefore, in order to determine the DMD modes corresponding to the kinetic energy growth within the flow field, DMD is performed only on the "near-equilibrium" region (Chen *et al.* 2012) of the snapshot kinetic energy (KE_{snap}). The "near-equilibrium" here refers to a partial regime of the transient state connecting one equilibrium state (the initial undisturbed separated flow) to another equilibrium state (nonlinear saturation), where the oscillation amplitude of this transient state is growing or decaying exponentially in time.

The definition of the kinetic energy density (KE) and the snapshot kinetic energy (KE_{snap}) in the PIV measurement window are given as follows,

$$KE(i, j, k) = \frac{M}{2}(U(i, j, k)^2 + V(i, j, k)^2) \quad (3.6)$$

where KE is the kinetic energy density, U is the horizontal velocity and V is the vertical velocity. The index i, j denote the coordinates in the 2-D measurement window, k is the snapshot number or discretized time series and M is the fluid density. Note that M is a constant number and does not change through out the entire space and time, therefore we let M equals to 1 without losing any generality.

$$KE_{snap}(k) = \sum_{i=1, j=1}^{m, n} KE(i, j, k) \quad (3.7)$$

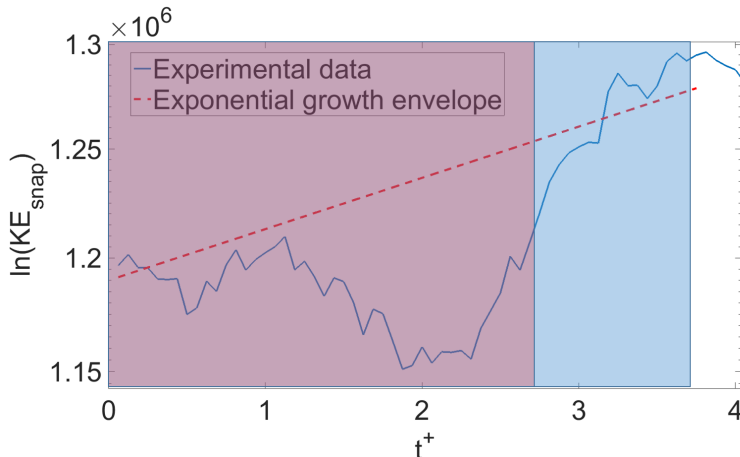


Figure 13: Snapshot kinetic energy, The blue window indicates the end of the exponential growth (near-equilibrium) region, and DMD is performed within the red window.

$KE_{snap}(k)$ is the snapshot kinetic energy, which is the total kinetic energy contained in the entire measurement window at each PIV snapshot k . The indices $m = 400$ and $n = 400$ denote the total number of the spatial points in horizontal and vertical direction, respectively. Here we just let each area represented by i, j to be 1 since all the grid points are equally spaced and does not change through out the entire space and time. Note that DMD analysis is performed on the kinetic energy density, KE . The snapshot kinetic energy KE_{snap} is only used to determine the "near-equilibrium" region. From figure 13, one can tell that the oscillation amplitude of the snapshot kinetic energy grows exponentially from $0t^+$ right after the burst signal until $3.3t^+$. Therefore, the DMD was performed on the kinetic energy density from $0t^+$ to $2.7t^+$.

The DMD modes are sorted in descending order of the kinetic energy contained in each spatial mode. The eigenvalues of the first 22 DMD modes are shown in figure 14. The horizontal axis is the imaginary part of the complex eigenvalues and the vertical axis is the real part of the complex eigenvalues. There is only one pair of complex conjugate modes (mode 7 and mode 8) associated with the positive real components of the eigenvalues ($3.75 \pm 27.60i$). These two modes are able to capture almost 60% of the disturbance kinetic energy in the flow field (figure 15), which indicates that these two modes are responsible for the kinetic energy growth. The corresponding frequency of this pair of modes is 4.4Hz ($F^+ \approx 0.36$), where $F^+ = fc/U_\infty$, f is the frequency in 'Hz', c is the chord length in 'meters' and U_∞ is the freestream speed in 'm/s'. The real components of the spatial and temporal evolution of these two DMD modes are shown in figure 16 a-b.

Based on the stability analysis of the flow field response to the single-burst actuation, one would simply assume that continuous actuation at the vicinity of $F^+ = 0.36$ will cause maximum energy absorbing from the freestream and hence, the maximum lift increment. However, this is not true due to the strong burst-burst interaction observed by An *et al.* (2016). The multi-burst actuation will be studied next.

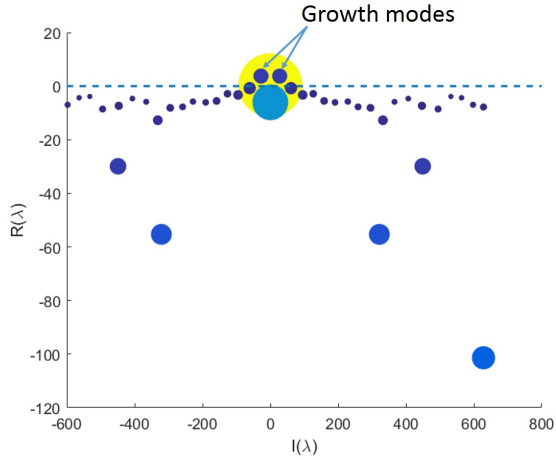


Figure 14: Eigenvalues computed from DMD on the kinetic energy density, mode 7 and mode 8 are marked by the arrows.

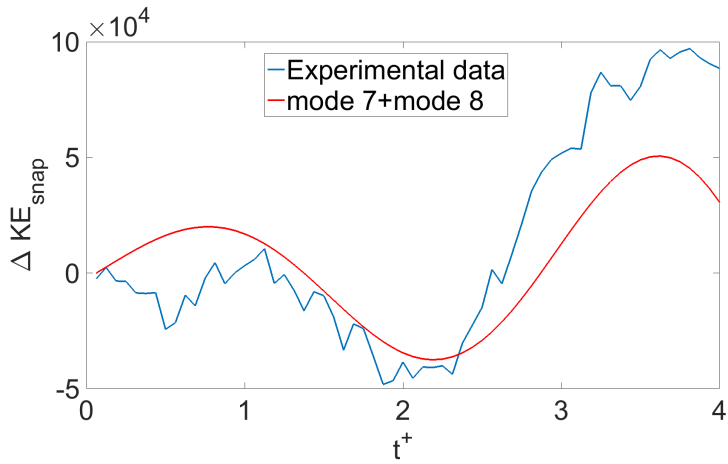


Figure 15: Comparison of the experimental ΔKE_{snap} and the reconstructed ΔKE_{snap} by mode 7 and mode 8. Here "Δ" indicates the disturbed value in which the non-actuated baseline value has been subtracted from the original data.

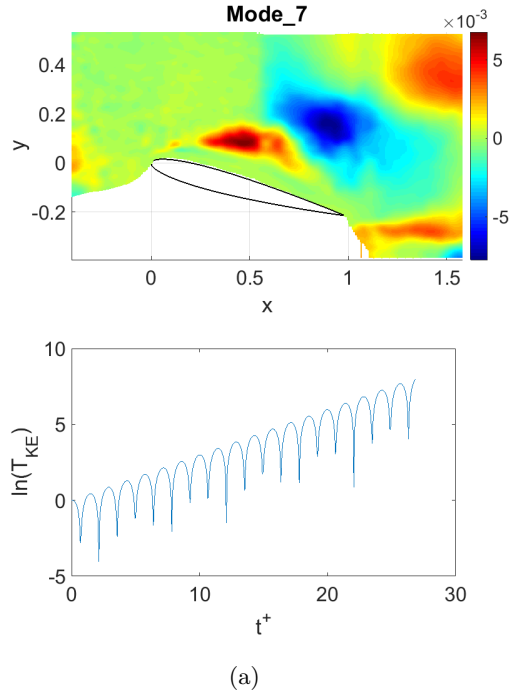


Figure 16: The growth mode, mode 7, the temporal coefficient T_{KE} is plotted in log scale.

4. Multi-burst Actuation

In common applications of dynamic active flow control, a continuous sequence of bursts is amplitude modulated to provide variable strength control. For example, dynamic stall vortex control on a pitching airfoil will require a time-varying burst amplitude during the airfoil maneuver. If linear dynamics governed the burst-mode response, then a convolution integral using the single-pulse response as a kernel in the integral should be sufficient to predict the lift response to an arbitrary actuator input. We expect this will be the case when the bursts are sufficiently far apart in time that interactions between single pulses are small. On the other hand, as the time between bursts decreases, then we expect interactions to occur between the current burst and the previous bursts, which will cause deviations from the convolution integral prediction. In this section the interactions between sequences of 10 bursts with different time intervals between their individual bursts are examined to determine the boundaries between linear and nonlinear behavior.

The 10 burst sequence is long enough to allow a steady state lift response to be reached. Five burst frequencies ($F^+ = 0.145, 0.29, 0.58, 0.65, 0.82$) were investigated. The lift coefficient increment ΔC_L following a sequence of 10 bursts is shown in figure 17 for three frequencies, $F^+ = 0.29, 0.58, 0.82$. The initial lift reversal is the same for the first burst in all three cases. After the initial burst, the lift increment quickly reaches a new steady state value (local mean) that is superposed with large amplitude oscillations at the burst frequency. From the lift coefficient increment data in figure 17, one observes that both the local mean and the amplitude of the ΔC_L oscillations depend on the burst frequency. The largest frequency $F^+ = 0.82$ has the lowest lift fluctuation level, and the lowest frequency $F^+ = 0.29$ has the largest lift fluctuation levels. The intermediate burst frequency $F^+ = 0.58$ has the largest average lift increment $\Delta C_L = 0.28$. The lift recovery after the final (10th) burst is the same for all three cases shown.

The local mean and the root mean square (rms) value of the ΔC_L response are plotted in figure 18. The dependence of the local mean value of ΔC_L on the burst frequency F^+ is plotted in figure 18a. The local mean value of ΔC_L is calculated by averaging the ΔC_L between the fourth and the ninth burst, so that it is not affected by the initial or final transients. The rms of ΔC_L (with the mean subtracted) is plotted in figure 18b. This value is also calculated between the fourth and ninth bursts to avoid the transient region on the burst-burst interaction.

Figure 18a shows that the maximum local mean of ΔC_L occurs in the vicinity of $F^+ \approx 0.58$. Raju *et al.* (2008) reported that maximum lift increment occurs when the actuation frequency is close to the subharmonic of the separation bubble frequency f_{sep}^+ . In the current research, $f_{sep}^+ \approx U_\infty/L_{sep} \cdot c/U_\infty$, where L_{sep} is the separation bubble length. Since the baseline flow is fully separated, we assume $L_{sep} = c$, so $f_{sep}^+ \approx 1$. Hence, the burst frequency, $F^+ \approx 0.58$, corresponding to the mean ΔC_L peak is close to the first subharmonic of the separation bubble frequency (figure 18a), which is in agreement with Raju *et al.* (2008).

However, the peak mean ΔC_L frequency ($F^+ \approx 0.58$) differs from the DMD growth mode frequency ($F^+ \approx 0.36$) from the single-burst case. This suggests that the instability triggered by the single-burst is not the only factor for the mean ΔC_L in the multi-burst actuation cases. The burst-burst interaction plays an important role as well. It is also worth of pointing out that figure 18a clearly shows that the relation between the mean ΔC_L and the actuation frequency is nonlinear.

On the other hand, within the frequency range considered, figure 18b shows that the rms of ΔC_L associated with the firing of each individual burst, decreases monotonically as the burst frequency increases.

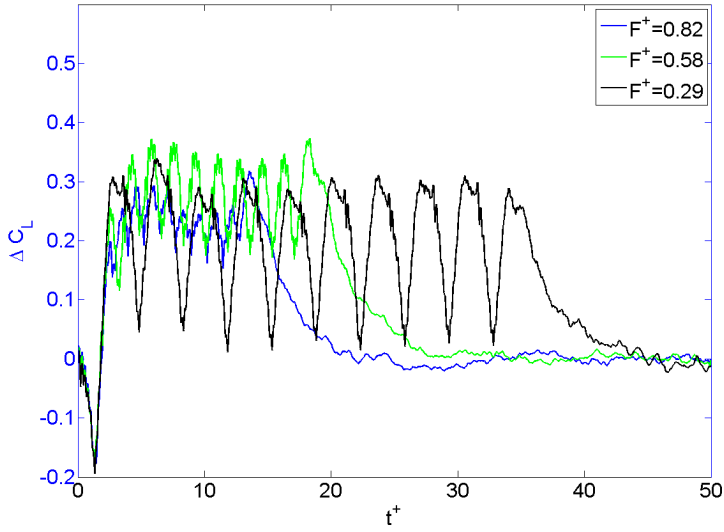


Figure 17: A ten-burst actuation sequence with different actuation frequencies.

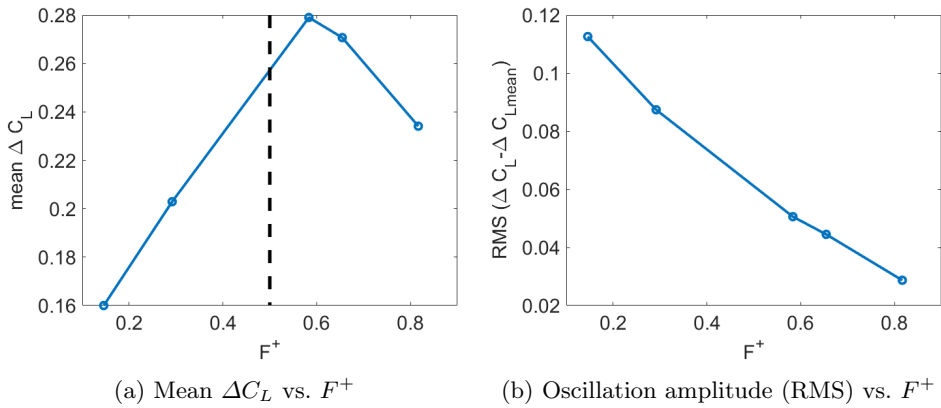


Figure 18: Actuation frequency effect on the mean ΔC_L and the oscillation amplitude (RMS), the black dashed line in (a) indicates the first subharmonic of the separation bubble frequency f_{sep}^+ .

To help clarify the differences between linear and nonlinear behavior during the multi-burst actuation, the convolution integral that uses a linear superposition of a sequence of the single-burst actuation was performed. If the flow responds linearly to the multi-burst input, then the convolution approach will predict the lift response. Differences between the linear convolution predictions and the actual measurements are assumed to be the result of nonlinear effects. Here we use the ΔC_L response from the single-burst as the kernel for the convolution integral, which is written in discrete form as

$$\Delta C_L(k) = \sum \Delta C_{L,single}(j)v(k-j). \quad (4.1)$$

$\Delta C_{L,single}$ is the C_L response to the single-burst with its baseline value subtracted, and $v(k)$ is the input voltage to the actuator at the time step k .

Figures 19a - 19d compare measurements with the convolution integral predictions of the lift increment response following a single burst and three multi-burst cases with different time delays between the bursts. Figure 19a shows that it takes approximately 20 convective times for the lift to return to its original state. When the second burst occurs before $t^+ = 20$, then the kernel begins at a non-zero initial value, and this leads to an artificial increase in the predicted lift increment. The lift increment for the second burst begins at a higher value than the first burst. The same effect occurs for the third burst relative to the second, and so on. In general, when the bursts are close together in time, e.g., $1.25 t^+$ figure 19b, then the convolution overpredicts the value of ΔC_L relative to the measured data. This phenomenon indicates that when the bursts are close to each other, the nonlinear burst-burst interaction effects become stronger.

In the case of figure 19b this leads to a large over-estimation in the maximum ΔC_L . However, as the time delay between pulses increases, then the lift increment from the first pulse has decayed closer to $\Delta C_L = 0$, and the convolution model overshoot is not as large.

The high-frequency component of the ΔC_L signal that is associated with the multi-burst signal is predicted reasonably well by the convolution integral. This similarity indicates that the high-frequency oscillation is dominated by the linear dynamics. Combining the low-frequency component of the signal with the high frequency oscillations of ΔC_L dependency on the frequency mentioned above, we can assume that there are two components to the burst-burst interaction. The nonlinear component of the burst-burst interaction affects the mean value of ΔC_L and the linear burst-burst interaction corresponds to the RMS or the high-frequency oscillation of ΔC_L . To further test this assumption, a more detailed investigation on the multi-burst flowfield is discussed next.

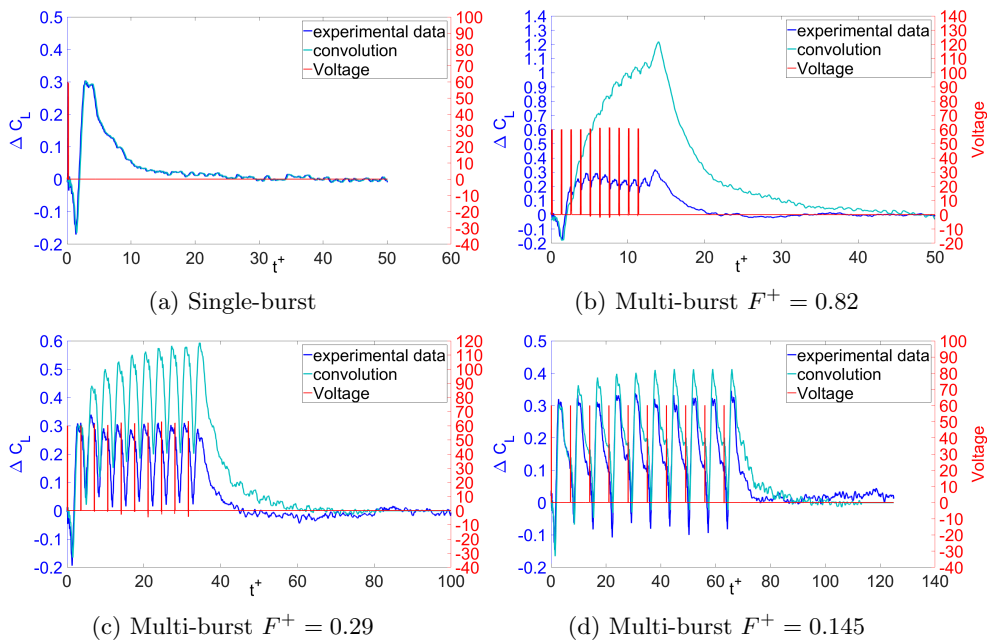


Figure 19: ΔC_L response to single-burst and multi-burst actuation at $\alpha = 12^\circ$. The red lines show the voltage to the actuators. a) single burst; b) 10 repeating bursts at $F^+ = 0.82$; c) 10 repeating bursts at $F^+ = 0.29$; d) 10 repeating bursts at $F^+ = 0.145$.

4.1. $F^+ = 0.82$ multi-burst actuation

The lift coefficient response to actuation is an integral effect from the overall flow field. To gain more insight into the mechanisms of the burst-burst interactions, phase-averaged flow field maps over the airfoil were acquired. Inspired by the convolution integral approach on the ΔC_L , we found that comparing the convolution integral simulated data with the directly measured data is an effective way of evaluating the linear-nonlinear character of the flow.

A procedure similar to the convolution integral method is applied to the velocity field data. The kernel in Eq. 4.1 is replaced by the flowfield evolution following the single-burst actuation. The input signal $V(k)$ is a 3-D (2 spatial dimensions and one dimension in time) variable, which means it is a spatially uniformly distributed matrix and only varying with time. For example, at the discrete time instant k , the flowfield is a 400×400 matrix. The input is $V(400 \times 400)$ with all the elements equal to one (if the burst occurs at time k) or zero (if it is between the bursts). The convolution integral of the flowfield can be expressed as follows,

$$\psi^{i,j,k} = \sum \psi_{single}^{i,j,m} V^{i,j,k-m} \quad (4.2)$$

where $\psi^{i,j,k}$ is the velocity at spatial location i, j in the k^{th} snapshot, $\psi_{single}^{i,j,m}$ is the velocity at spatial location i, j in the m^{th} snapshot for the single-burst actuation case, and $V^{i,j,k-m}$ is the input signal at spatial location i, j in the $(k-m)^{th}$ snapshot.

The convolution integral is applied to the $F^+ = 0.82$ multi-burst case, which is the actuation with the highest burst frequency. This case shows the strongest burst-burst interaction. The results are organized into three columns in figure 20. The first

column contains the lift coefficient increment with a dashed vertical line marking the time corresponding to each row. The second and third columns show the PIV direct measured flowfield (DMF) and the convolution simulated flowfield (CSF), respectively. The vortex structure is plotted on top of the velocity vectors in columns two and three.

We expect the DMF and CSF flowfields to be similar at short times after the onset of actuation, when the measured and convolution simulated ΔC_L in figure 20 are similar, because the flowfield evolution is responsible for the ΔC_L variation. At times $0.0t^+$, $2.0t^+$, and $2.7t^+$ shown in the first three rows of figure 20, one can observe similarities in the flow field structures of concentrated vorticity. To provide more detail, the dashed black line shown in figure 20a denotes the instant at $0t^+$ where the ΔC_L has not been disturbed. The DMF at $0t^+$ is shown in figure 20b and the CSF is shown in figure 20c. The DMF and CSF exhibit a very strong similarity at $0t^+$, since the burst signal was not triggered yet. At $2t^+$ after the initializing of the burst signal, the DMF still shows a strong similarity compared to the CSF despite the firing of the second burst, as it is shown in figure 20e and figure 20f. The ΔC_L plotted at $2t^+$ (figure 20d) exhibits the same trend as the flowfield, the direct measured and convolution simulated ΔC_L is very close. After $2.7t^+$ the CSF starts to deviate from the DMF, and so do the direct measured and the convolution simulated ΔC_L (figure 20g to figure 20o).

At the time $4.0t^+$ (fourth row) the predicted lift increment begins to deviate from the measured lift, and the directly measured and convolution simulated flow fields are also different. In particular, the measured flow field shows a well organized vortex at the trailing edge that is not reproduced by the convolution approach.

In order to better understand the differences between the directly measured flow and the convolution simulated flow, we will first try to explain the CSF. In the single-burst case there are two distinct time scales. The vortex formation and shedding that contribute to the initial lift reversal, and the following ΔC_L increment occurs in a short time scale ($O(1)t^+$) as shown in figure 9a to figure 9g. But the process of recovery to the original undisturbed separated flow takes much longer ($O(10)t^+$), which is shown in figure 9g and figure 9h. This asymmetric ΔC_L response (in terms of time required for C_L to increase and decrease) following the single-burst actuation leads to the overprediction of C_L in the multi-burst case when the convolution method is used for prediction.

In a multi-burst sequence the first burst produces the detached leading edge vortex (DLEV) which begins to convect downstream. The second burst in the sequence will not directly affect the DLEV, because the actuation occurs upstream of the convecting DLEV. But if the second burst occurs before the flowfield has returned to its non-excited condition (which takes about $10t^+$), then the initial condition for the lift coefficient increment in the second burst is larger than zero in the convolution integral. The process repeats for each successive burst, and the lift coefficient increment continues to increase artificially until the burst sequence is complete.

In reality in a multi-burst sequence, the directly measured flowfield indicates that the second burst indeed has a strong influence on the reattached shear layer caused by the previous burst. It breaks the previous burst-induced reattached shear layer into two parts, and attempts to establish a new reattachment. On the other hand, in the DMF, the upstream current burst-induced vortex formation and advection will have a weaker influence on the downstream DLEV caused by the previous burst, which is similar to the CSF.

Taking a close look at figure 20h to figure 20o, one can observe that the clockwise rotational vortices' location and strength for both DMF and CSF show a certain level of similarity. But there is a high velocity region that covers the entire chord length above the upper surface of the wing in the CSF (figure 20i, figure 20l and figure 20o) which

differs from the DMF (figure 20h, figure 20k and figure 20n). This high-speed region is also in response of producing the counterclockwise rotational vortices above the trailing-edge (at $y/c \approx 0.1$) in CSF. Therefore, one can speculate that the high-speed region above the wing in the CSF contributes to a higher mean lift increment than the DMF. The difference between the CSF and the DMF on this high-speed region implies the nonlinear portion of burst-burst interaction. But the similar clockwise rotating vortex structure within the DMF and CSF produces similar high-frequency periodic oscillation associated with the burst signal in ΔC_L , which indicates the linear portion of burst-burst interaction. Next, to quantitatively analyze the linear and nonlinear dynamics of the multi-burst actuation, we will decompose the flowfield into different modes based on their dynamic characteristics.

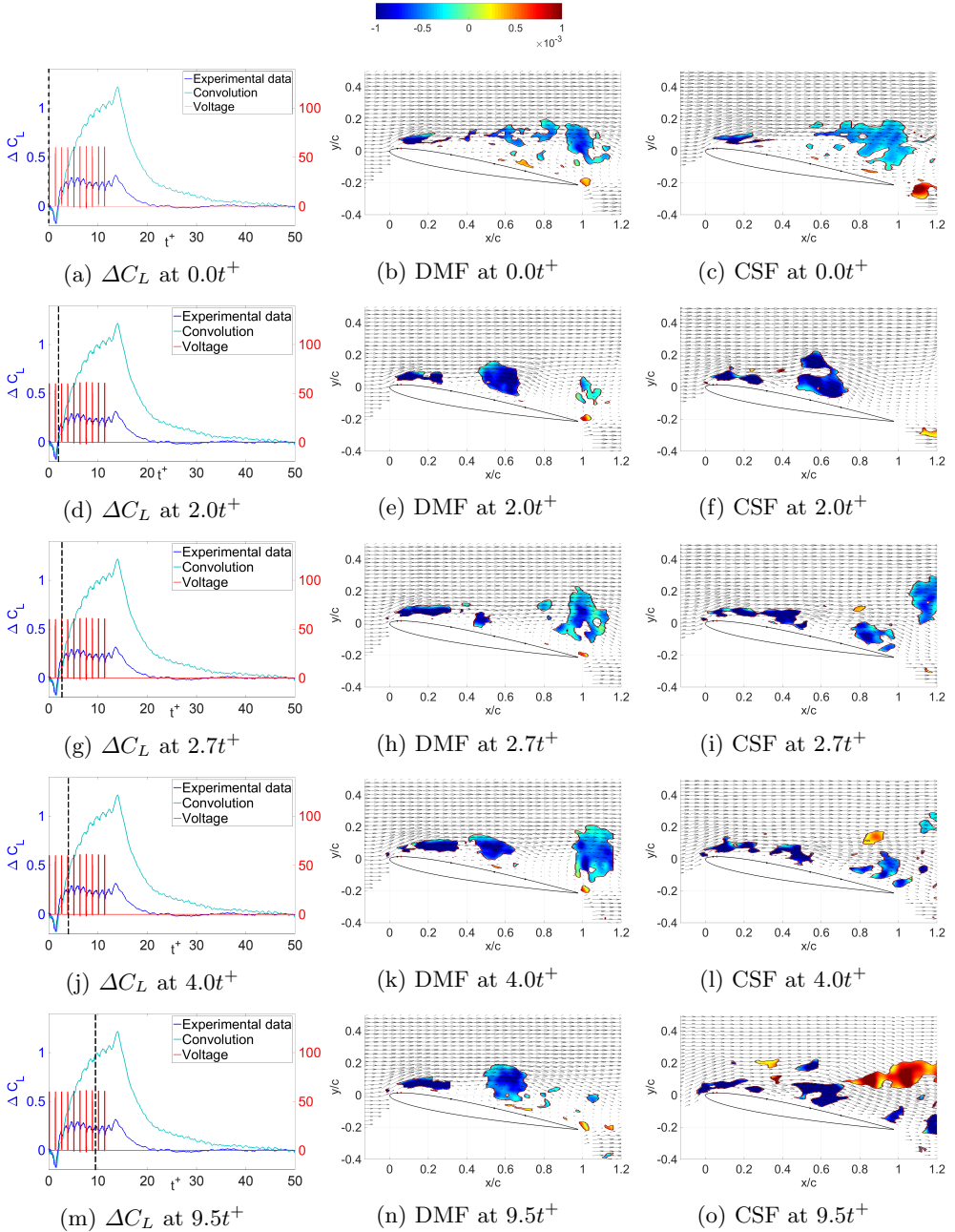


Figure 20: Comparison of DMF and CSF, the burst frequency is $F^+ = 0.82$, which is equivalent to $1.25t^+$ burst interval. The figures on the left are the directly measured and convolution simulated ΔC_L (solid deep blue line and solid cyan), corresponding to the multi-burst input signal (solid red line). The dashed black lines indicate the instants associated with the DMF (in the middle) and the CSF (on the right), the black arrows indicate the velocity vectors and the color contour indicates the vortex strength.

4.2. Dynamic modal analysis for DMF and CSF

The singular value decomposition (SVD) based dynamic mode decomposition (DMD) (Rowley *et al.* 2009) (Schmid 2010) (Tu *et al.* 2013) was employed to identify the dynamic modes for both the DMF and the CSF. In general, DMD is not suitable for the dynamic system containing nonlinear transitions. However, if the nonlinear transition only occurs once from one equilibrium state to another, then this transition may be approximated by decaying oscillating modes, whose initial value is "1" and the final value is "0". Hence, DMD was performed on the velocity field of the $F^+ = 0.82$ multi-burst cases from $0t^+$ to $12t^+$, it can be seen that there is only one transitional event from $0t^+$ to $12t^+$ in figure 19b.

The eigenvalues of the critical DMD modes of the DMF and the CSF are shown in table 1 and table 2. The critical modes of both cases are defined as those which can reconstruct the original dataset with the least number of modes. Table 3 shows the correlation coefficients of the spatial modes between DMF and CSF. Table 4 shows the correlation coefficients of the temporal coefficients associated with the spatial modes between DMF and CSF.

Mode 0	Mode 2	Mode 14	Mode 18
-0.0010+0.0000i	-7.8899+9.2895i	-3.6004-8.1792i	-0.0827-62.9156i

Table 1: Eigenvalues of DMF's DMD modes.

Mode 0	Mode 1	Mode 8	Mode 18
0.0253+0.0000i	-2.5608+0.0000i	-0.2786-62.2852i	-4.6605-16.1187i

Table 2: Eigenvalues of CSF's DMD modes.

Table 3 exhibits a strong similarity between spatial mode 0 from DMF and spatial mode 0 from CSF. However, one could argue that they are different if we compare the spatial modes in figure 21a and figure 21b. In fact, the high similarity is due to a large portion of these two modes that only contains the freestream flow, which is not affected by the actuation. However, the high-speed flow in CSF tends to be more attached than that in the DMF. This phenomenon partially contributes to the main trend of the ΔC_L difference for these two cases shown in figure 19b. The correlation coefficient between the temporal coefficients of mode 0 from DMF and CSF is 1 (figure 22a and figure 22b), since both of them are the linearly growth/decay modes without periodic oscillation, the temporal coefficients are linearly dependent.

Table 3, also shows that the spatial mode 1 in the CSF is similar to the spatial mode 2 in the DMF despite the velocity magnitude difference. Combining the temporal coefficients (figure 22c and figure 22d) and these two spatial modes, they imply that both of these two modes from CSF and DMF represent the reduction of the reverse flow within in the separation region. However, figure 21c and figure 21d exhibit that the velocity reduction magnitude of CSF mode 1 is larger than DMF mode 2. This contributes to the different ΔC_L increment magnitude in figure 19b between the direct measurement and the convolution integral. The more interesting feature of these two modes is that their temporal coefficients approximately track the main trend of the ΔC_L in figure 19b respectively. The magnitude difference in these two spatial modes and the trend difference in their temporal coefficients indicate the main trend of the ΔC_L variation of the multi-burst actuation is due to the nonlinear burst-burst interaction.

Figure 21e, figure 22e, figure 21f and figure 22f show that both mode 18 in CSF and mode 14 in DMF are responsible for reverse flow reduction within the separation region, although the correlation between these two modes is relative weak (Table 3 and Table 4).

Nevertheless, the most interesting modes are mode 18 from the DMF and mode 8 from the CSF. There is a strong correlation between these two modes (Table 3 and table 4). The oscillation frequencies of these two modes are $F^+ \approx 0.82$ (figure 22g and figure 22h), which is the same as the burst frequency. More importantly, figure 21g and Fig 21h exhibit that these two modes are responsible for the actuation induced vortex evolution. This is important evidence that the CSF is able to capture the vortex evolution in DMF, which is in response to the high-frequency ($F^+ = 0.82$) flowfield/ ΔC_L oscillation. Hence, convolution or linear superposition of the single-burst actuation response is capable of tracking the high-frequency (burst frequency) component of the multi-burst actuation. Moreover, as it was previously mentioned, the nonlinear burst-burst interaction (mode

DMF \ CSF	Mode 0	Mode 1	Mode 8	Mode 18
Mode 0	0.7766	0.1105	0.0543	0.2291
Mode 2	0.5223	0.7192	0.0425	0.3462
Mode 14	0.2883	0.4415	0.1557	0.1588
Mode 18	0.0114	0.0382	0.6656	0.0371

Table 3: Correlation coefficients between DMF and CSF, the spatial modes from DMD

DMF \ CSF	Mode 0	Mode 1	Mode 8	Mode 18
Mode 0	1	0.9545	0.0190	0.1798
Mode 2	0.4804	0.6711	0.0369	0.7758
Mode 14	0.3773	0.6011	0.0209	0.5650
Mode 18	0.0383	0.0328	0.9451	0.0259

Table 4: Correlation coefficients between DMF and CSF, the temporal coefficients of the modes from DMD

2 of DMF and mode 1 of CSF) has a strong connection to the main trend of the ΔC_L curve rather than the high-frequency oscillation. These important features provide us a guideline for the modeling of ΔC_L variation related to the multi-burst or the continuous burst actuation in future research.

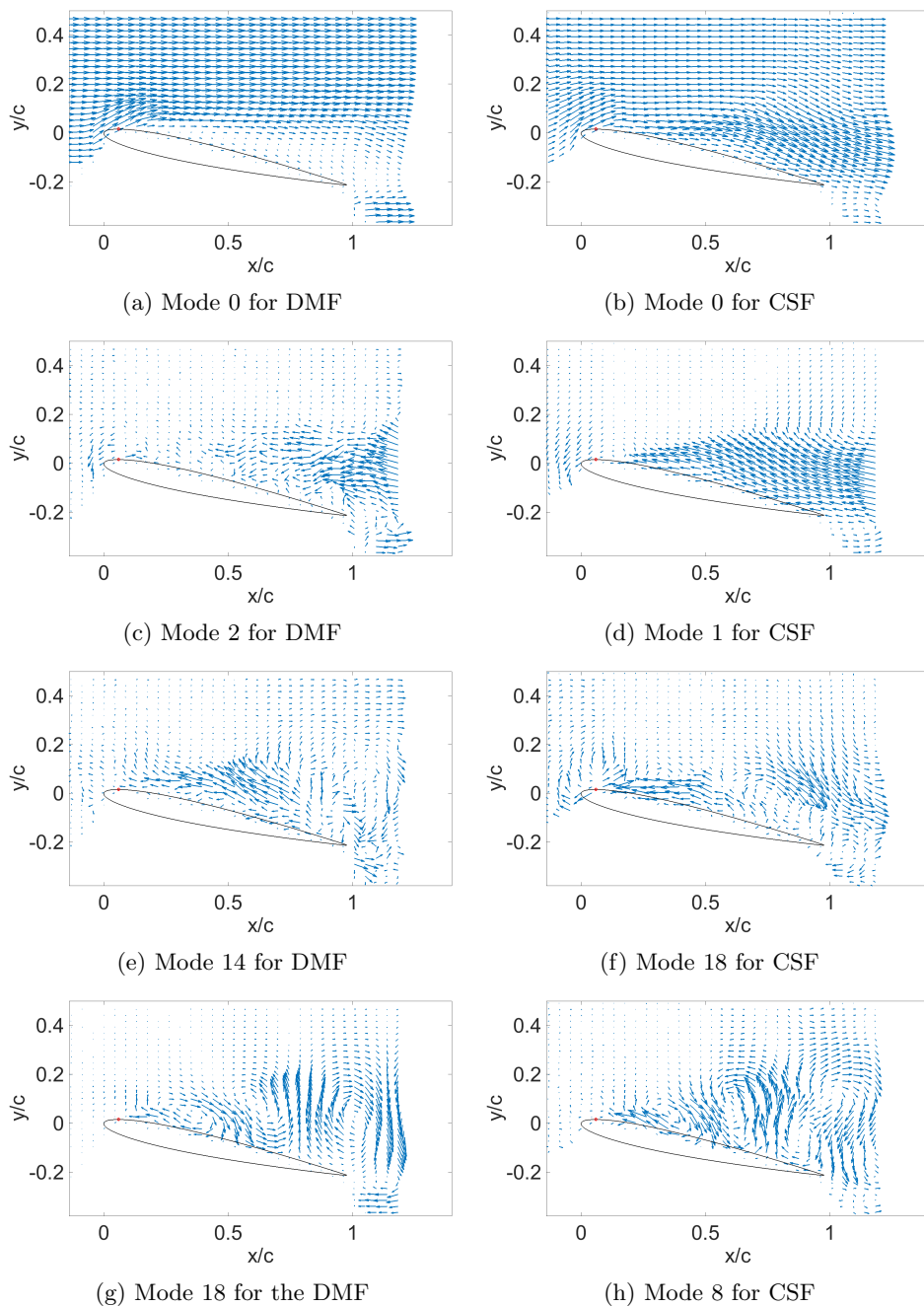


Figure 21: The comparison of the spatial DMD modes from the DMF and CSF. The arrows in each figure indicate the velocity magnitude and direction

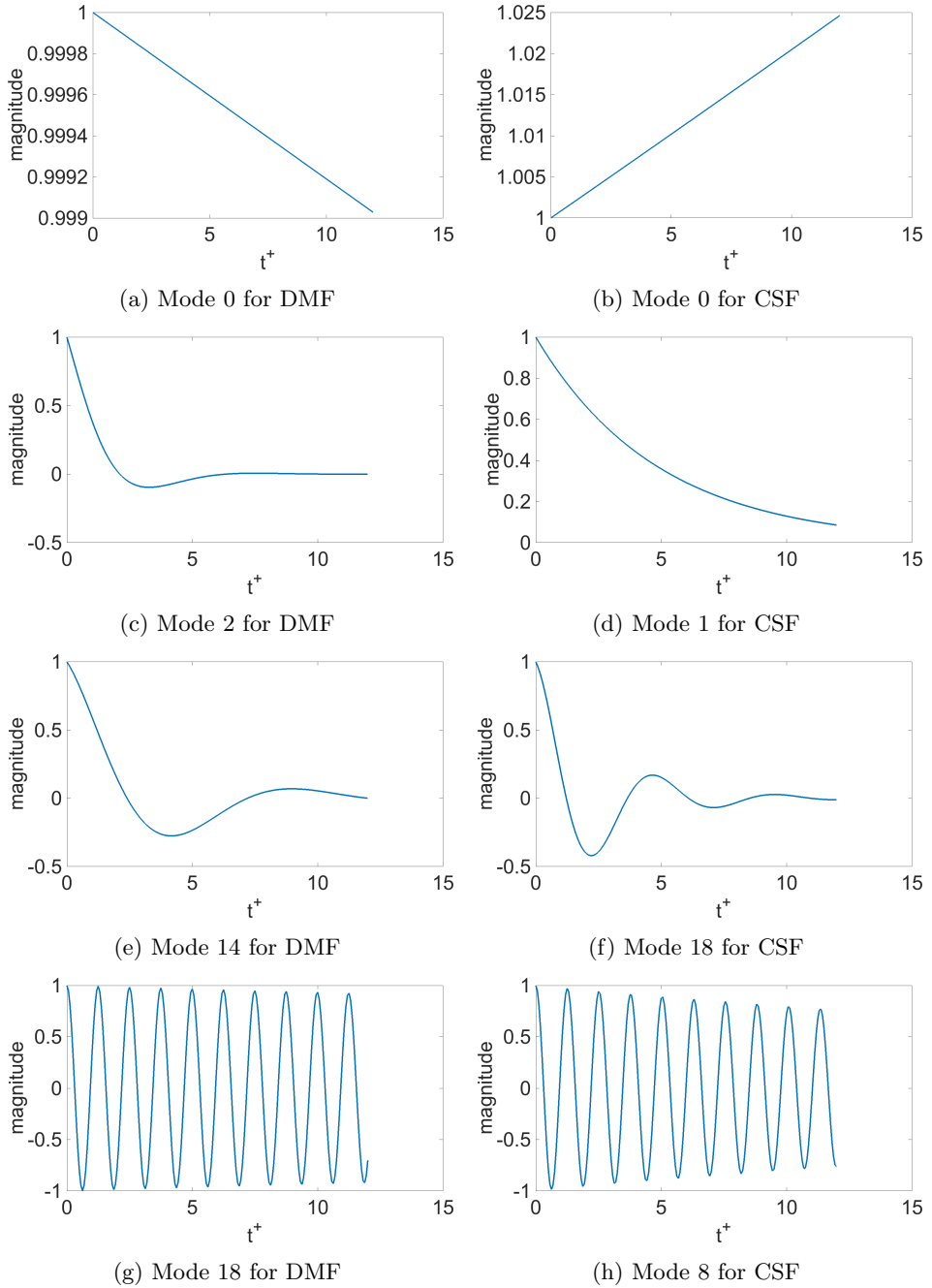


Figure 22: The comparison of the temporal coefficients of the DMD modes from DMF and CSF.

5. Conclusion

In this work, the naturally separated flow over an NACA-0009 wing responding to single-burst and multi-burst actuation was investigated. Both the time-evolving flow structure, lift, pitching moment, and their dynamic characteristics were studied. The work is applicable to actuator design, actuation parameter selection and low-order modeling of the time-varying lift for flow control applications.

When the separated flow is perturbed by a single-burst actuation, the streamlines of the flowfield demonstrate the reattachment process corresponding to the lift coefficient variation. There is a downwash impacting on the suction side of the wing that moves with the clockwise rotating large-scale leading edge vortex. This results in a pressure increase, and leads to an initial lift reversal before the DLEV convects into the wake. The maximum lift reversal is observed at $1.4t^+$ after initiation of the single-burst, and the maximum lift increment occurs at $2.8t^+$, when the flow is reattached. The POD analysis shows that most of the disturbed kinetic energy is stored in mode 1 and mode 2. The combined temporal coefficients of POD mode 1 and mode 2 track the negative lift coefficient curve, especially during the lift reversal. Unlike the lift coefficient curve, there is no obvious positive increment observed in the pitching moment coefficient, and it is closely tracked by the temporal coefficient of the POD mode 2. Stability analysis on the kinetic energy density field following the single-burst actuation shows that the DMD modes at $F^+ \approx 0.36$ are responsible for the kinetic energy growth within the measurement window.

The investigations of the multi-burst actuation showed that the maximum mean lift gain occurs at the burst frequency $F^+ \approx 0.58$, which is close to the first subharmonic of the separation bubble frequency ($F^+ \approx 1$), but differs from the growth DMD mode of the single-burst actuation ($F^+ \approx 0.36$). This is important evidence that the maximum lift gain is determined by a combination of single-pulse triggered instability and the burst-burst interaction. The mean ΔC_L dependency on the burst frequency is nonlinear process, while the RMS or the high oscillation amplitude (corresponding to the firing of the bursts) of ΔC_L dependency on the burst frequency can be modelled with a linear convolution method within the frequency range that has been investigated.

The convolution integral on the multi-burst actuation flowfield was performed to investigate the interactions occurring between the bursts. The comparison of DMD modes between DMF and CSF indicates that the nonlinear burst-burst interaction has a strong influence on the main trend of the time-varying flowfield/lift. On the other hand, the high-frequency oscillations associated with the burst frequency strongly depend on the linear burst-burst interaction. These important features provide a guideline for the modeling of ΔC_L variation related to the multi-burst or the continuous burst actuation in future research.

REFERENCES

- AMITAY, MICHAEL & GLEZER, ARI 2002a Controlled transients of flow reattachment over stalled airfoils. *International Journal of Heat and Fluid Flow* **23** (12), 690–699.
- AMITAY, MICHAEL & GLEZER, ARI 2002b Controlled transients of flow reattachment over stalled airfoils. *International Journal of Heat and Fluid Flow* **23** (5), 690–699.
- AMITAY, MICHAEL & GLEZER, ARI 2006 Flow transients induced on a 2d airfoil by pulse-modulated actuation. *Experiments in Fluids* **40** (2), 329–331.
- AN, XUANHONG, WILLIAMS, DAVID R, ELDRIDGE, JEFF D & COLONIUS, TIM 2016 Modeling dynamic lift response to actuation. In *54th AIAA Aerospace Sciences Meeting*, p. 0058.
- BRZOWSKI, DAN, WOO, GEORGE TK, CULP, JOHN R & GLEZER, ARI 2010 Transient separation control using pulse-combustion actuation. *AIAA journal* **48** (5), 2482.

- CHEN, KEVIN K, TU, JONATHAN H & ROWLEY, CLARENCE W 2012 Variants of dynamic mode decomposition: boundary condition, koopman, and fourier analyses. *Journal of nonlinear science* **22** (6), 887–915.
- FAGE, ARTHUR & JOHANSEN, FC 1927 On the flow of air behind an inclined flat plate of infinite span. *Proc. R. Soc. Lond. A* **116** (773), 170–197.
- GRAFTIEAUX, LAURENT, MICHARD, MARC & GROSJEAN, NATHALIE 2001 Combining piv, pod and vortex identification algorithms for the study of unsteady turbulent swirling flows. *Measurement Science and technology* **12** (9), 1422.
- JEONG, JINHEE & HUSSAIN, FAZLE 1995 On the identification of a vortex. *Journal of fluid mechanics* **285**, 69–94.
- KERSCHEN, GAETAN, GOLINVAL, JEAN-CLAUDE, VAKAKIS, ALEXANDER F & BERGMAN, LAWRENCE A 2005 The method of proper orthogonal decomposition for dynamical characterization and order reduction of mechanical systems: an overview. *Nonlinear dynamics* **41** (1), 147–169.
- KERSTENS, WESLEY, PFEIFFER, JENS, WILLIAMS, DAVID, KING, RUDIBERT & COLONIUS, TIM 2011 Closed-loop control of lift for longitudinal gust suppression at low reynolds numbers. *AIAA journal* **49** (8), 1721–1728.
- KERSTENS, WESLEY, WILLIAMS, DAVID, PFEIFFER, JENS, KING, RUDIBERT & COLONIUS, TIM 2010 Closed loop control of a wing's lift for 'gust' suppression. *5th Flow Control Conference, AIAA Paper 2010-4969* .
- MONNIER, BRUNO, WILLIAMS, DAVID R, WEIER, TOM & ALBRECHT, THOMAS 2016 Comparison of a separated flow response to localized and global-type disturbances. *Experiments in Fluids* **57** (7), 1–16.
- PRASAD, ANIL & WILLIAMSON, CHARLES HK 1996 The instability of the separated shear layer from a bluff body. *Physics of Fluids* **8** (6), 1347–1349.
- RAJU, RENI, MITTAL, RAJAT & CATTAFESTA, LOUIS 2008 Dynamics of airfoil separation control using zero-net mass-flux forcing. *AIAA journal* **46** (12), 3103.
- RIVAL, DAVID E, KRIEGSEIS, JOCHEN, SCHAUB, PASCAL, WIDMANN, ALEXANDER & TROPEA, CAMERON 2014 Characteristic length scales for vortex detachment on plunging profiles with varying leading-edge geometry. *Experiments in fluids* **55** (1), 1660.
- ROWLEY, CLARENCE W, MEZIĆ, IGOR, BAGHERI, SHERVIN, SCHLATTER, PHILIPP & HENNINGSON, DAN S 2009 Spectral analysis of nonlinear flows. *Journal of fluid mechanics* **641**, 115–127.
- SCHMID, PETER J 2010 Dynamic mode decomposition of numerical and experimental data. *Journal of fluid mechanics* **656**, 5–28.
- STROUHAL, VINCENZ 1878 Über eine besondere art der tonerregung. *Annalen der Physik* **241** (10), 216–251.
- TU, JONATHAN H, ROWLEY, CLARENCE W, LUCHTENBURG, DIRK M, BRUNTON, STEVEN L & KUTZ, J NATHAN 2013 On dynamic mode decomposition: theory and applications. *arXiv preprint arXiv:1312.0041* .
- WILLIAMS, DAVID R, AN, XUANHONG, ILIEV, SIMEON, KING, RUDIBERT & REISSNER, FLORIAN 2015 Dynamic hysteresis control of lift on a pitching wing. *Experiments in Fluids* **56** (5), 112.
- WILLIAMS, DAVID R & KING, RUDIBERT 2018 Alleviating unsteady aerodynamic loads with closed-loop flow control. *AIAA Journal* **56** (6), 2194–2207.
- WOO, GEORGE, CRITTENDEN, THOMAS & GLEZER, ARI 2009 Transitory separation control over a stalled airfoil. *AIAA paper* **4281**, 2009.
- WOO, GEORGE T. K., CRITTENDEN, THOMAS M. & GLEZER, ARI June 2008 Transitory control of a pitching airfoil using pulse combustion actuation. *4th Flow Control Conference, AIAA Paper 2008-4324* .